IET Electric Power Applications

Research Article

IET Journals
The Institution of Engineering and Technology

Characteristic analysis and direct measurement for air gap magnetic field of external rotor permanent magnet synchronous motors in electric vehicles

ISSN 1751-8660
Received on 13th November 2019
Revised 7th March 2020
Accepted on 12th May 2020
E-First on 4th August 2020
doi: 10.1049/iet-epa.2019.0931
www.ietdl.org

Conggan Ma[1,2], Shengsen Zhou[1], Na Yang[1], Michele Degano[2] ✉, Christopher Gerada[2], Jianguang Fang[3], Qinghe Liu[1]

[1]*School of Automotive Engineering, Harbin Institute of Technology-Weihai, Weihai, People's Republic of China*
[2]*Department of Electrical and Electronic Engineering, the University of Nottingham, Nottingham NG7 2RD, UK*
[3]*School of Civil and Environmental Engineering, the University of Technology Sydney, Sydney, Australia*
✉ *E-mail: michele.degano@nottingham.ac.uk*

Abstract: In this study, the air gap magnetic field characteristics of external rotor permanent magnet synchronous motors (PMSMs) under both the stator and rotor coordinate systems considering low-order current harmonics and high-order sideband current harmonics are analysed. A direct measurement technique (DMT) for air-gap magnetic field is proposed. First, an analytical model of air gap magnetic field of external rotor PMSMs is established. The spatial order and frequency characteristics of stator/rotor air gap magnetic field are revealed. Then, a 24-pole 27-slot external rotor PMSM is taken as an example. The analytical and finite element (FE) results are compared and analysed. The difference of the spatial order and frequency characteristics between the stator and rotor air gap magnetic field are verified. Next, a new DMT is proposed, which can detect the precise distribution and local microscopic characteristics on the order of 10^{-1} mm with high resolution. The accuracy of analytical and FE model are verified by the DMT and an indirect experimental test of no-load back electromotive force. Finally, the mechanical challenges of in-wheel motors and the practicablility of DMT for eccentricity detection are further discussed.

1 Introduction

The driving form of in-wheel motors becomes one of the ultimate driving forms of electric vehicles because of short transmission chain, high transmission efficiency and good control performance. External rotor permanent magnet synchronous motors (PMSMs) with high-efficiency and high-energy density becomes the main type of in-wheel motors. The air gap is the main place for electromechanical energy conversion of external rotor PMSMs, and air gap magnetic field determines the output performance of motors.

On one hand, for an inner rotor PMSM, the external stator is the radiator of electromagnetic noise. As it is stationary, the magnetic field on its inner surface is mainly influenced by the pole-pairs of the rotational rotor. On the other hand, for an external rotor PMSM studied in this work, the external rotor connects to the wheel hub of electric vehicle. It rotates and meanwhile radiates the electromagnetic noise. The magnetic field on its inner surface is mainly affected by the slots of the stationary stator. In other words, the electromagnetic excitation characteristics of an external rotor PMSM are significantly different from that of an inner rotor PMSM. In addition, its PWM inverter generates amount of low-order current harmonics and high-order sideband current harmonics in the phase currents. All of the current harmonics further amplify the differences between the electromagnetic excitation characterisitics of an external rotor PMSM and an inner rotor PMSM. Therefore, it is of great significance to study the air gap magnetic field characteristics of external rotor PMSMs under both the stator and rotor coordinate systems considering low-order current harmonics and high-order sideband current harmonics.

At present, there are three main research methods of air gap magnetic field: analytical method, finite element (FE) method and measurement method. The analytical method mainly includes subdomain method and magnetic potential magnetic permeability method. The subdomain method generally divides the motor into subdomains and solves the Laplace equation or Poisson equation through the boundary conditions between the sub-fields to obtain the air gap magnetic field distribution. In [1–3] the subdomain method were used to calculate the no-load air gap magnetic field of the surface-mounted permanent magnet (PM) motors, those models were verified by FE method. In [4, 5], the no-load and load magnetic fields of the spoke-type motor were calculated, respectively. The models were verified by the FE method. The magnetic potential magnetic permeability method obtains the air gap magnetic field distribution by multiplying the magnetic potential without considering the slotting effect and the magnetic permeability considering the slotting effect. The literature [6, 7] used the one-dimensional (1D) magnetic potential permeability method to solve the magnetic field distribution of the motor, but only considers the change of the magnetic conductance in the circumferential direction. The literature [8–11] used the 2D magnetic potential magnetic permeability method to calculate the no-load and load magnetic field considers the variation of the magnetic conductance along circumference and radial direction. However, the above two methods can only predict radial magnetic density and cannot predict tangential magnetic density. In [9], the concept of complex relative permeability was proposed. The real and imaginary parts of the complex permeability were considered to account for the air gap magnetic field distortion caused by the slotting. The analytical model can accurately calculate the radial magnetic density and the tangential magnetic density. In literature [12–15], the complex relative permeability model was used to consider the effect of stator slotting, and the no-load magnetic field or load magnetic field is analytically calculated. However, they did not consider the magnetic field characteristics in the rotor coordinate system.

The calculation time of analytical method is short, which can directly reveal the general variation law of air gap magnetic field of the motor with same type, but the theoretical derivation process is extremely complicated. The FE method [16, 17] can solve air gap magnetic field more accurately, but it is time consuming and not

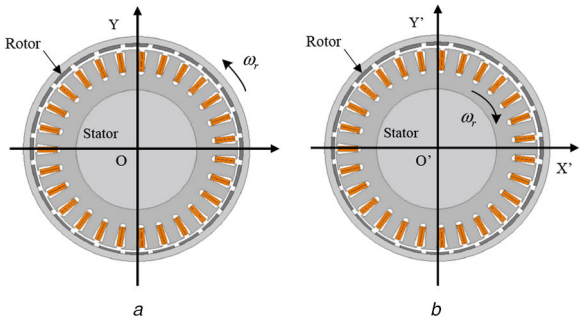

Fig. 1 *The coordinate system of external rotor PMSMs*
(a) Stator static coordinate *XOY*, ***(b)*** Rotor motion

possible to directly reveal the variation law of air gap magnetic field of the motors with same type.

The air gap is generally very narrow and is only about 10^{-1} mm long. For the measurement methods for air gap magnetic fields, there are currently two main types: direct measurement methods [18–20] and indirect measurement methods [7, 21, 22]. The direct measurement mainly uses a linear Hall-effect flux sensor to directly detect the air gap magnetic field distribution. In [18], a Hall sensor that can be attached to the stator surface was used to measure the air gap flux of an axial flux motor. In [19], 36 Hall flux sensors were installed in the air gap to detect the rotor fault and eccentricity of the rotor. In [20], the flux density was measured using a combination of eight linear Hall-effect flux sensors and a rotary encoder. However, the requirements for the size and detection method of linear Hall-effect flux sensors are extremely high due to the air gap. Therefore, most of the existing researches use the indirect measurement method of air gap magnetic field. The indirect measurement method mainly proves the accuracy of the calculation of air gap magnetic field by testing the no-load back electromotive force (EMF), cogging torque and electromagnetic torque. In [21], the induced EMF of the coil and the winding were first tested, the air gap magnetic field were calculated then. The disadvantage of indirect measurement is that it cannot verify the spatial distribution and order characteristics of the magnetic field.

In summary, the research on characteristic analysis and measurement methods for air gap magnetic field has the following drawbacks:

(i) The existing papers have not thoroughly revealed the spatial order and frequency characteristics of both the stator and rotor air gap magnetic field of external rotor PMSMs, especially considering the PWM technique.
(ii) Most of the existing papers compare the analytical calculation result with the FE result to judge the accuracy. This evaluation method is not accurate enough, asboth the FE and analytical calculation require some assumptions. In addition, both FE and analytical calculation method cannot accurately detect the actual air gap magnetic field distribution law in design stage of motors, which will greatly increase the motor development cost.
(iii) The time-domain magnetic field can be verified by the above-mentioned direct or indirect measurement methods respectively, but the spatial location and local distribution characteristics of magnetic field faults cannot directly be detected. In addition, the difference in the axial distribution of the magnetic field cannot directly be diagnosed.

Therefore, the analytic model and FE model of air gap magnetic field of external rotor PMSMs under stator static and rotor motion coordinate systems with PWM technique are established by using magnetic potential magnetic permeability method. The spatial order and frequency characteristics of stator and rotor air gap magnetic field are revealed, respectively. A new direct measurement method for air gap magnetic field is proposed. The analytical and FE results are verified by direct measurement for air gap magnetic field and indirect measurement method of the no-load back EMF.

This study is arranged as follows: In Section 2, the analytical model of air gap magnetic field of external rotor PMSMs under stator static and rotor motion coordinate systems with PWM technique are established by using magnetic potential magnetic permeability method, respectively. In Section 3, the space-time distribution characteristics of air gap magnetic field in stator static/rotor motion coordinate systems are analysed by using analytical and FE methods. In Section 4, the equipment composition and method of the direct measurement for air gap magnetic field are proposed, the direct measurement of air gap magnetic field and the indirect measurement method of no-load back EMF are used to verify the accuracy of analytical and FE results. In Section 5, the mechanical challenges of in-wheel motors are discussed and the practicablility of direct measurement technique (DMT) for eccentricity detection is verified.

2 Analytical model

2.1 Stator static coordinate and rotor motion coordinate

For an external rotor PMSM used as in-wheel motor of electric vehicle, the external rotor is connected to the hub, and the inner stator is connected to suspension. The mechanical properties of rotor and stator greatly affect the dynamic performance of electric vehicles. Figs. 1*a* and *b* are schematic diagrams of stator static coordinate system *XOY* and rotor motion coordinate system *X′O′Y′* of external rotor PMSMs, respectively. For the rotor coordinate system *X′O′Y′*, the coordinate system is fixed to the rotor, which is equivalent to the rotor being stationary and the stator rotating in the opposite direction.

2.2 Assumed conditions and input current

The analytical model in this study is based on the following assumptions:

(i) The magnetic flux density vector has only radial and tangential component, and contains no axial component.
(ii) The flux saturation is neglected.
(iii) The PM is magnetised radially.

When applying PWM technique, the current harmonics of external rotor PMSMs mainly consists of two parts: the low frequency current harmonics $(3h \pm 1)f_c$ and PWM sideband frequency current harmonics $k_1 f_s \pm k_2 f_c$, where h, k_1 and k_2 are positive integers. The phase-A current expression is

$$i_A(t) = I_c \sin(2\pi f_c t + \theta_c) + \sum_{h \in N^*} I_{3h\pm1} \sin(2\pi f_{3h\pm1} t + \theta_{3h\pm1}) + \sum_{k_1 \in N^*, k_2 \in N^*} I_{k_1 f_s \pm k_2 f_c} \sin\left[2\pi(k_1 f_s \pm k_2 f_c)t + \theta_{k_1 f_s \pm k_2 f_c}\right] \quad (1)$$

where I_c, $I_{3h\pm1}$ and $I_{k_1 f_s \pm k_2 f_c}$ represent the amplitude of current fundamental, $(3h \pm 1)f_c$ harmonics and $k_1 f_s \pm k_2 f_c$ harmonics, respectively, f_s and f_c represent the switching frequency and fundamental frequency, respectively.

According to the symmetry of the winding, the current expressions of phase-B and phase-C can be easily obtained.

2.3 Air gap magnetic field in stator static coordinate system

In the stator stationary coordinate system, the air gap radial and tangential magnetic fields of the external rotor PMSMs are [8, 9, 12, 22]

(see (2))

(see (3))

where B_{r_s} and B_{t_s} represent the radial and tangential magnetic fields in the stator coordinate system, respectively. B_{ru_s} and B_{tu_s} represent the radial and tangential magnetic fields without considering slotting, respectively. λ_a and λ_b represent the real and imaginary part of the complex relative permeability of the slotting effect, B_{Mru_s} and B_{Mtu_s} represent the radial and tangential

$$
\begin{aligned}
B_{\mathrm{r\_s}}(r,\theta,t) &= B_{\mathrm{ru\_s}}(r,\theta,t)\lambda_{\mathrm{a}}(\theta) + B_{\mathrm{tu\_s}}(r,\theta,t)\lambda_{\mathrm{b}}(\theta) \\
&= [B_{\mathrm{Mru\_s}}(r,\theta,t) + B_{\mathrm{Aru\_s}}(r,\theta,t)]\lambda_{\mathrm{a}}(\theta) \\
&\quad + [B_{\mathrm{Mtu\_s}}(r,\theta,t) + B_{\mathrm{Atu\_s}}(r,\theta,t)]\lambda_{\mathrm{b}}(\theta) \\
&= \left\{ \begin{array}{l} \displaystyle\sum_{n=1,3,5\ldots}^{\infty} B_{\mathrm{Mrk}}(r) \times \cos[np(\theta - \omega t - \theta_0)] \\ \displaystyle + \sum_{v=1}^{\infty} B_{\mathrm{rv}} \sum_{m=1}^{3} i_m(t) \sum_{n=1}^{N} S_{mi} \cos v\left[m\theta - \frac{2\pi}{Q_0}(\theta_{mi} - 1)\right] \end{array} \right\} \\
&\quad \times \left[\lambda_0 + \sum_{\eta=1}^{N_\lambda} \lambda_{a\eta} \cos(\eta Q_{\mathrm{s}}\theta)\right] \\
&\quad + \left\{ \begin{array}{l} \displaystyle\sum_{n=1,3,5\ldots}^{\infty} B_{\mathrm{Mtk}}(r) \times \sin[np(\theta - \omega t - \theta_0)] \\ \displaystyle + \sum_{v=1}^{\infty} B_{tv} \sum_{m=1}^{3} i_m(t) \left\{ \sum_{n=1}^{N} S_{mi} \sin v\left[m\theta - \frac{2\pi}{Q_0}(\theta_{mi} - 1)\right] \right\} \end{array} \right\} \\
&\quad \times \sum_{\eta=1}^{N_\lambda} \lambda_{b\eta} \sin(\eta Q_{\mathrm{s}}\theta)
\end{aligned} \tag{2}
$$

$$
\begin{aligned}
B_{\mathrm{t\_s}}(r,\theta,t) &= B_{\mathrm{tu\_s}}(r,\theta,t)\lambda_{a}(\theta) - B_{\mathrm{ru\_s}}(r,\theta,t)\lambda_{\mathrm{b}}(\theta) \\
&= [B_{\mathrm{Mtu\_s}}(r,\theta,t) + B_{\mathrm{Atu\_s}}(r,\theta,t)]\lambda_{\mathrm{a}}(\theta) \\
&\quad - [B_{\mathrm{Mru\_s}}(r,\theta,t) + B_{\mathrm{Aru\_s}}(r,\theta,t)]\lambda_{\mathrm{b}}(\theta) \\
&= \left\{ \begin{array}{l} \displaystyle\sum_{n=1,3,5\ldots}^{\infty} B_{\mathrm{Mtk}}(r) \times \sin[np(\theta - \omega t - \theta_0)] \\ \displaystyle + \sum_{v=1}^{\infty} B_{\mathrm{tv}} \sum_{m=1}^{3} i_m(t) \left\{ \sum_{n=1}^{N} S_{mi} \cos v\left[m\theta - \frac{2\pi}{Q_0}(\theta_{mi} - 1)\right] \right\} \end{array} \right\} \\
&\quad \times \left[\lambda_0 + \sum_{\eta=1}^{N_\lambda} \lambda_{a\eta} \cos(\eta Q_{\mathrm{s}}\theta)\right] \\
&\quad - \left\{ \begin{array}{l} \displaystyle\sum_{n=1,3,5\ldots}^{\infty} B_{\mathrm{Mrk}}(r) \times \cos[np(\theta - \omega t - \theta_0)] \\ \displaystyle + \sum_{v=1}^{\infty} B_{\mathrm{rv}} \sum_{m=1}^{3} i_m(t) \left\{ \sum_{n=1}^{N} S_{mi} \cos v\left[m\theta - \frac{2\pi}{Q_0}(\theta_{mi} - 1)\right] \right\} \end{array} \right\} \\
&\quad \times \sum_{\eta=1}^{N_\lambda} \lambda_{b\eta} \sin(\eta Q_{\mathrm{s}}\theta)
\end{aligned} \tag{3}
$$

Table 1 Spatial order and frequency characteristics in stator coordinate system

Source	Spatial order	Frequency characteristic
$B_{\mathrm{Mu\_s}} \times \lambda_0$	np	nf_{c}
$B_{\mathrm{Mu\_s}} \times \lambda_a$	$np \pm \eta Q_{\mathrm{s}}$	nf_{c}
$B_{\mathrm{Mu\_s}} \times \lambda_{\mathrm{b}}$	$np \pm \eta Q_{\mathrm{s}}$	nf_{c}
$B_{\mathrm{Au\_s}} \times \lambda_0$	vm	$(3h \pm 1)f_{\mathrm{c}},\ k_1 f_{\mathrm{s}} \pm k_2 f_{\mathrm{c}}$
$B_{\mathrm{Au\_s}} \times \lambda_a$	$vm \pm \eta Q_{\mathrm{s}}$	$(3h \pm 1)f_{\mathrm{c}},\ k_1 f_{\mathrm{s}} \pm k_2 f_{\mathrm{c}}$
$B_{\mathrm{Au\_s}} \times \lambda_{\mathrm{b}}$	$vm \pm \eta Q_{\mathrm{s}}$	$(3h \pm 1)f_{\mathrm{c}},\ k_1 f_{\mathrm{s}} \pm k_2 f_{\mathrm{c}}$

magnetic field of the PM without considering slotting, respectively. $B_{\mathrm{Aru\_s}}$ and $B_{\mathrm{Atu\_s}}$ represent the radial and tangential armature reaction magnetic field without considering the slot, respectively. m represents the number of unit motors.

When the phase current $i_m(t) = 0$, (2) and (3) are the no-load radial and tangential magnetic fields, respectively. According to those formulas, the spatial order and frequency characteristics of air gap magnetic field in stator coordinate system of external rotor PMSMs can be derived, as shown in Table 1.

2.4 Air gap magnetic field in rotor motion coordinate system

In rotor motion coordinate system, the external rotor is stationary with respect to coordinate system. The PM magnetic field is a function of the spatial angle, the complex relative permeability is a function of two variables, time and spatial angle. The air gap radial and tangential magnetic fields of external rotor PMSMs with PWM technique can be expressed as [8, 9, 12, 22]

(see (4))

(see (5))

where in rotor coordinate system, $B_{\mathrm{r\_r}}$, $B_{\mathrm{t\_r}}$, $B_{\mathrm{ru\_r}}$, $B_{\mathrm{tu\_r}}$, $B_{\mathrm{Mru\_r}}$, $B_{\mathrm{Mtu\_r}}$, $B_{\mathrm{Aru\_r}}$, $B_{\mathrm{Atu\_r}}$, $\lambda_{\mathrm{r\_a}}$ and $\lambda_{\mathrm{r\_b}}$ correspond to the respective quantities in stator coordinate system.

The spatial order and frequency characteristics of the air gap magnetic field in rotor coordinate system of external rotor PMSMs are derived from those formulas, as shown in Table 2.

2.5 Difference of magnetic field between stator and rotor coordinate systems

According to Tables 1 and 2, it can obviously be found that the spatial order characteristics of the magnetic field in the stator and rotor coordinate systems are the same. However, their frequency components are different, as shown in Table 3. Therefore, this kind of difference should be taken into consideration especially when

Table 2 Spatial order and frequency characteristics in rotor coordinate system

Source	Spatial order	Frequency characteristic
$B_{\mathrm{Mu\_r}} \times \lambda_0$	np	0
$B_{\mathrm{Mu\_r}} \times \lambda_a$	$np \pm \eta Q_\mathrm{s}$	$\eta Q_\mathrm{s} f_\mathrm{r}$
$B_{\mathrm{Mu\_r}} \times \lambda_b$	$np \pm \eta Q_\mathrm{s}$	$\eta Q_\mathrm{s} f_\mathrm{r}$
$B_{\mathrm{Au\_r}} \times \lambda_0$	vm	$(3h \pm 1) f_\mathrm{c} \pm v f_\mathrm{r},\ k_1 f_\mathrm{s} \pm k_2 f_\mathrm{c} \pm v f_\mathrm{r}$
$B_{\mathrm{Au\_r}} \times \lambda_a$	$vm \pm \eta Q_\mathrm{s}$	$(3h \pm 1) f_\mathrm{c} \pm (v \pm \eta Q_\mathrm{s}) f_\mathrm{r},\ k_1 f_\mathrm{s} \pm k_2 f_\mathrm{c} \pm (v \pm \eta Q_\mathrm{s}) f_\mathrm{r}$
$B_{\mathrm{Au\_r}} \times \lambda_b$	$vm \pm \eta Q_\mathrm{s}$	$(3h \pm 1) f_\mathrm{c} \pm (v \pm \eta Q_\mathrm{s}) f_\mathrm{r},\ k_1 f_\mathrm{s} \pm k_2 f_\mathrm{c} \pm (v \pm \eta Q_\mathrm{s}) f_\mathrm{r}$

Table 3 Comparison of frequency characteristics between stator and rotor coordinate system

Source	Stator coordinate	Rotor coordinate
$B_{\mathrm{Mu\_r}} \times \lambda_0$	$n f_\mathrm{c}$	0
$B_{\mathrm{Mu\_r}} \times \lambda_a$	$n f_\mathrm{c}$	$\eta Q_\mathrm{s} f_\mathrm{r}$
$B_{\mathrm{Mu\_r}} \times \lambda_b$	$n f_\mathrm{c}$	$\eta Q_\mathrm{s} f_\mathrm{r}$
$B_{\mathrm{Au\_r}} \times \lambda_0$	$(3h \pm 1) f_\mathrm{c},\ k_1 f_\mathrm{s} \pm k_2 f_\mathrm{c}$	$(3h \pm 1) f_\mathrm{c} \pm v f_\mathrm{r},\ k_1 f_\mathrm{s} \pm k_2 f_\mathrm{c} \pm v f_\mathrm{r}$
$B_{\mathrm{Au\_r}} \times \lambda_a$	$(3h \pm 1) f_\mathrm{c},\ k_1 f_\mathrm{s} \pm k_2 f_\mathrm{c}$	$(3h \pm 1) f_\mathrm{c} \pm (v \pm \eta Q_\mathrm{s}) f_\mathrm{r},\ k_1 f_\mathrm{s} \pm k_2 f_\mathrm{c} \pm (v \pm \eta Q_\mathrm{s}) f_\mathrm{r}$
$B_{\mathrm{Au\_r}} \times \lambda_b$	$(3h \pm 1) f_\mathrm{c},\ k_1 f_\mathrm{s} \pm k_2 f_\mathrm{c}$	$(3h \pm 1) f_\mathrm{c} \pm (v \pm \eta Q_\mathrm{s}) f_\mathrm{r},\ k_1 f_\mathrm{s} \pm k_2 f_\mathrm{c} \pm (v \pm \eta Q_\mathrm{s}) f_\mathrm{r}$

$$
\begin{aligned}
B_{\mathrm{r\_r}}(r,\theta,t) &= B_{\mathrm{ru\_r}}(r,\theta,t)\lambda_{\mathrm{r\_a}}(\theta) + B_{\mathrm{tu\_r}}(r,\theta,t)\lambda_{\mathrm{r\_b}}(\theta) \\
&= [B_{\mathrm{Mru\_r}}(r,\theta,t) + B_{\mathrm{Aru\_r}}(r,\theta,t)]\lambda_{\mathrm{r\_a}}(\theta) \\
&\quad + [B_{\mathrm{Mtu\_r}}(r,\theta,t) + B_{\mathrm{Atu\_r}}(r,\theta,t)]\lambda_{\mathrm{r\_b}}(\theta) \\
&= \left\{ \begin{array}{l} \displaystyle\sum_{n=1,3,5\ldots}^{\infty} B_{\mathrm{Mrk}}(r) \times \cos[np(\theta+\theta_0)] \\ \displaystyle + \sum_{v=1}^{\infty} B_{rv} \sum_{m=1}^{3} i_m(t) \sum_{n=1}^{N} S_{mi} \cos v\left[\omega t + \varphi + m\theta - \frac{2\pi}{Q_0}(\theta_{mi}-1)\right] \end{array} \right\} \\
&\quad \times \left[\lambda_0 + \sum_{\eta=1}^{N_\lambda} \lambda_{a\eta} \cos \eta Q_\mathrm{s}(\omega t + \varphi + \theta)\right] \\
&\quad + \left\{ \begin{array}{l} \displaystyle\sum_{n=1,3,5\ldots}^{\infty} B_{\mathrm{Mtk}}(r) \times \sin[np(\theta+\theta_0)] \\ \displaystyle + \sum_{v=1}^{\infty} B_{\mathrm{tv}} \sum_{m=1}^{3} i_m(t) \left\{ \sum_{n=1}^{N} S_{mi} \sin v\left[\omega t + \varphi + m\theta - \frac{2\pi}{Q_0}(\theta_{mi}-1)\right] \right\} \end{array} \right\} \\
&\quad \times \sum_{\eta=1}^{N_\lambda} \lambda_{b\eta} \sin \eta Q_\mathrm{s}(\omega t + \varphi + \theta)
\end{aligned} \tag{4}
$$

$$
\begin{aligned}
B_{\mathrm{t\_r}}(r,\theta,t) &= B_{\mathrm{tu\_r}}(r,\theta,t)\lambda_{\mathrm{r\_a}}(\theta) - B_{\mathrm{ru\_r}}(r,\theta,t)\lambda_{\mathrm{r\_b}}(\theta) \\
&= [B_{\mathrm{Mtu\_r}}(r,\theta,t) + B_{\mathrm{Atu\_r}}(r,\theta,t)]\lambda_{\mathrm{r\_a}}(\theta) \\
&\quad - [B_{\mathrm{Mru\_r}}(r,\theta,t) + B_{\mathrm{Aru\_r}}(r,\theta,t)]\lambda_{\mathrm{r\_b}}(\theta) \\
&= \left\{ \begin{array}{l} \displaystyle\sum_{n=1,3,5\ldots}^{\infty} B_{\mathrm{Mtk}}(r) \times \sin[np(\theta+\theta_0)] \\ \displaystyle + \sum_{v=1}^{\infty} B_{\mathrm{tv}} \sum_{m=1}^{3} i_m(t) \left\{ \sum_{n=1}^{N} S_{mi} \cos v\left[\omega t + \varphi + m\theta - \frac{2\pi}{Q_0}(\theta_{mi}-1)\right] \right\} \end{array} \right\} \\
&\quad \times \left[\lambda_0 + \sum_{\eta=1}^{N_\lambda} \lambda_{a\eta} \cos \eta Q_\mathrm{s}(\omega t + \varphi + \theta)\right] \\
&\quad - \left\{ \begin{array}{l} \displaystyle\sum_{n=1,3,5\ldots}^{\infty} B_{\mathrm{Mrk}}(r) \times \cos[np(\theta+\theta_0)] \\ \displaystyle + \sum_{v=1}^{\infty} B_{\mathrm{rv}} \sum_{m=1}^{3} i_m(t) \left\{ \sum_{n=1}^{N} S_{mi} \cos v\left[\omega t + \varphi + m\theta - \frac{2\pi}{Q_0}(\theta_{mi}-1)\right] \right\} \end{array} \right\} \\
&\quad \times \sum_{\eta=1}^{N_\lambda} \lambda_{b\eta} \sin \eta Q_\mathrm{s}(\omega t + \varphi + \theta)
\end{aligned} \tag{5}
$$

Table 4 Main parameters of the motor

Items	Symbol	Value	Unit
rated speed	v_R	600	rpm
load torque	N_m	20	Nm
number of slots	Q_s	27	—
number of poles	$2p$	24	—
inner diameter of stator core	R_{s_i}	87.3	Mm
outer diameter of stator core	R_s	123.2	Mm
inner diameter of rotor core	R_r	128.0	Mm
outer diameter of rotor core	R_{r_o}	136.2	Mm

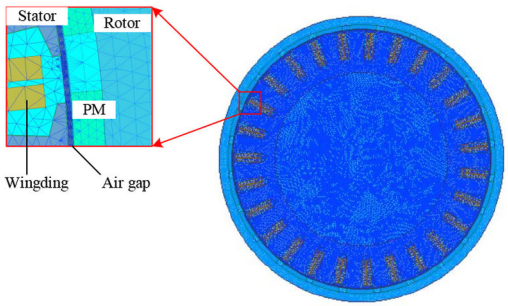

Fig. 2 *FE model of the external rotor PMSM*

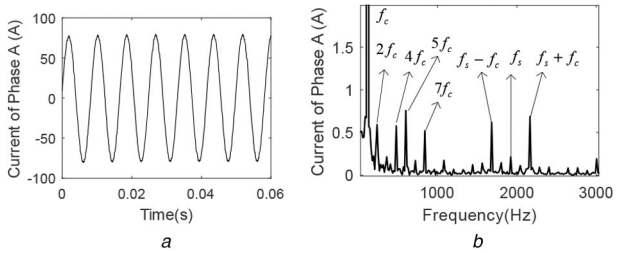

Fig. 3 *Phase-A current*
(a) Time history, ***(b)*** Amplitude–frequency

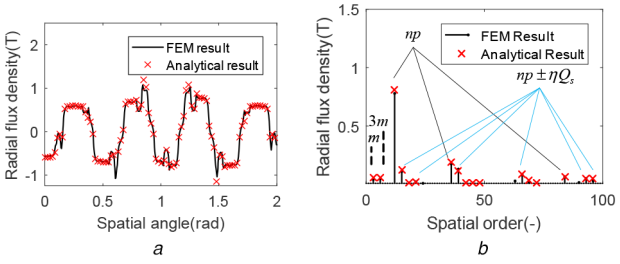

Fig. 4 *Spatial characteristics of radial magnetic field in stator static coordinate*
(a) Spatial distribution, ***(b)*** Amplitude-order

studying the electromagnetic excitation force, vibration, and noise of external rotor PMSM.

3 Characteristics of the magnetic field

In this study, a 24-pole 27-slot external rotor PMSM is taken as an example. The main parameters are shown in Table 4.

The characteristics of air gap magnetic field are analysed by the analytical model derived in Section 2 and the FE model (Fig. 2). First, the current generated by the PWM technique, which comes from external circuit from ANSYS Maxwell, is applied to the analytical and FE models. Fig. 3*a* and *b* are the time history diagram and amplitude–frequency characteristic of the phase-A current used in the model, respectively.

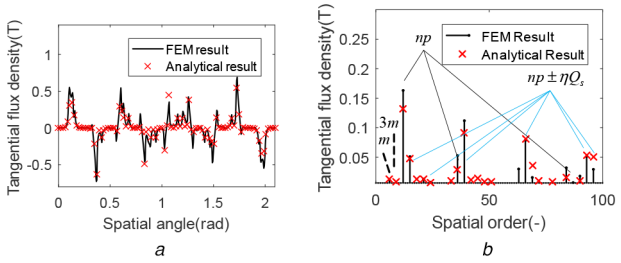

Fig. 5 *Spatial characteristics of tangential magnetic field in stator static coordinate*
(a) Spatial distribution, ***(b)*** Amplitude-order

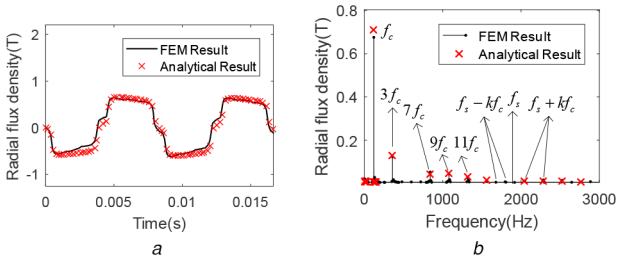

Fig. 6 *Time history of radial magnetic field in stator static coordinate*
(a) Time history, ***(b)*** Amplitude–frequency

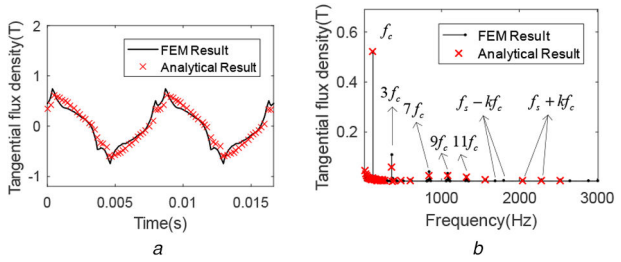

Fig. 7 *Time history of tangential magnetic field in stator static coordinate*
(a) Time history, ***(b)*** Amplitude–frequency

3.1 Characteristics in stator static coordinate system

In stator static coordinate system, the spatial order and frequency characteristics of the air gap magnetic field under the load torque of 20 Nm are analysed.

In stator static coordinate system, the analytical results have higher consistency with FE results, as shown in Figs. 4 and 5. The main spatial orders are: 12, 36 39, 42, 66, 84, etc., belong to np and $np \pm \eta Q_s$, generated by the PM magnetic field. Some of the smaller components 3, 6, etc., belong to vm and $vm \pm \eta Q_s$, generated by the armature reaction magnetic field.

The analytical result and the FE result of time history have high consistency as shown in Figs. 6 and 7. The main frequency components are: 120, 360, 840, 1080, 1320 Hz etc., which are generated by PM magnetic field ηf_c and armature reaction magnetic field $(3h \pm 1)f_c$. There are also some frequency components with smaller amplitudes, such as: 1680, 1800, 1920, 2040, 2160 Hz, etc. which belong to the PWM sideband frequency $k_1 f_s \pm k_2 f_c$.

The 2D fast Fourier transform (2D-FFT) decomposition method is used in this study, to simultaneously analyse the spatial order and frequency characteristics of the air gap magnetic field, as shown in Figs. 8 and 9. The main spatial order and frequency are $(f_c, np \pm \eta Q_s)$.

3.2 Characteristics in rotor motion coordinate system

In rotor motion coordinate system, the spatial order and frequency characteristics of the magnetic field are analysed. It can be seen from Figs. 10 and 11 that the analytical results have high consistency with the FE results, and the spatial order is the same as that of the stator static coordinate system.

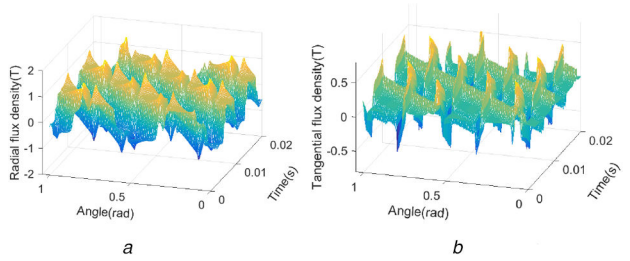

Fig. 8 *Spatial distribution and time history of magnetic field in stator static coordinate system*
(a) Radial, ***(b)*** Tangential

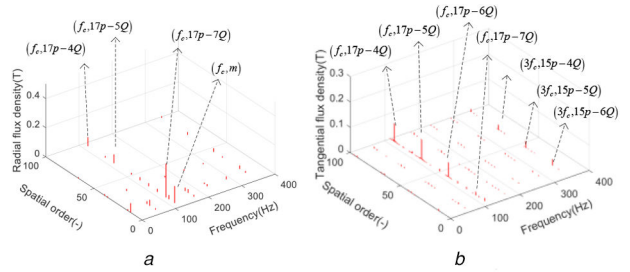

Fig. 9 *2D-FFT of magnetic field in stator static coordinate system*
(a) Radial, ***(b)*** Tangential

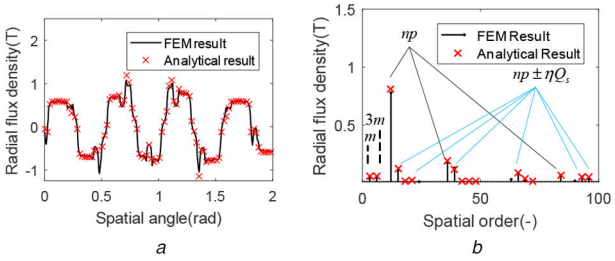

Fig. 10 *Spatial characteristics of radial magnetic field in rotor motion coordinate*
(a) Spatial distribution, ***(b)*** Amplitude-order

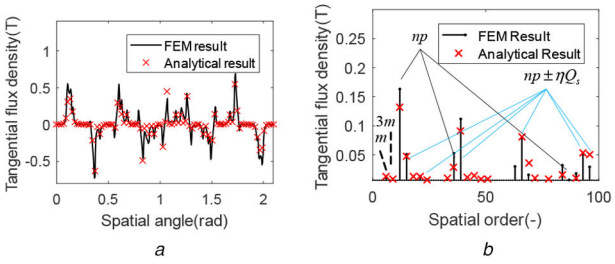

Fig. 11 *Spatial characteristics of tangential magnetic field in rotor motion coordinate*
(a) Spatial distribution, ***(b)*** Amplitude-order

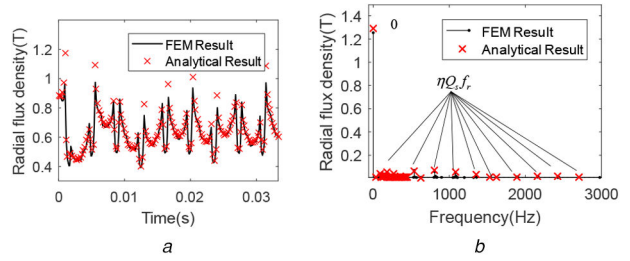

Fig. 12 *Time history of radial magnetic field in rotor motion coordinate*
(a) Time history, ***(b)*** Amplitude–frequency

The obvious difference is that the frequency components are different compared with the stator static coordinate system, as show in Figs. 12 and 13. The main frequency components are: 0, 540, 810, 1080, 1349 Hz, etc., belonging to 0 and $\eta Q_s f_r$

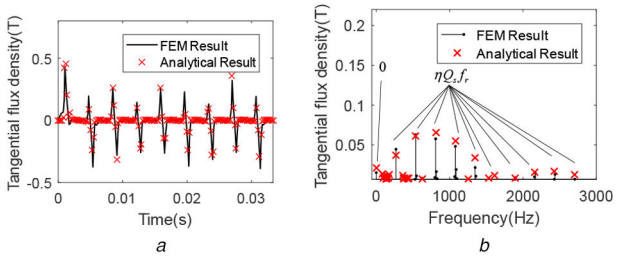

Fig. 13 *Time history of tangential magnetic field in rotor motion coordinate*
(a) Time history, ***(b)*** Amplitude–frequency

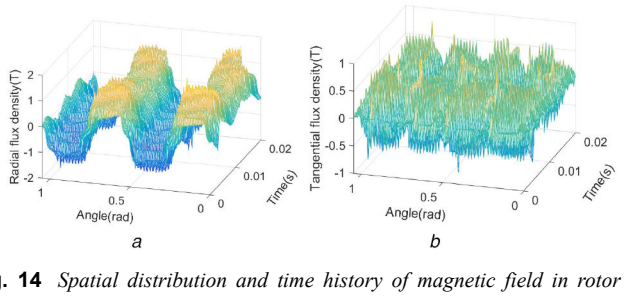

Fig. 14 *Spatial distribution and time history of magnetic field in rotor motion coordinate system*
(a) Radial, ***(b)*** Tangential

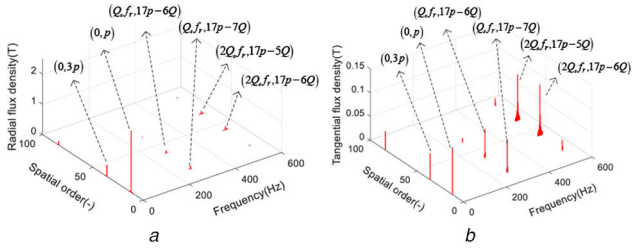

Fig. 15 *2D-FFT of magnetic field in rotor motion coordinate system*
(a) Radial, ***(b)*** Tangential

components generated by PM magnetic field, the frequency components with smaller amplitudes such as 90, 180, 360 Hz etc. belonging to the armature reaction magnetic field components $(3h \pm 1)f_c \pm vf_r$ and $(3h \pm 1)f_c \pm (v \pm \eta Q_s f_r)$. The switching frequency will also contribute to the composition $k_1 f_s \pm k_2 f_c \pm vf_r$ and $k_1 f_s \pm k_2 f_c \pm (v \pm \eta Q_s f_r)$, but the amplitude is small, which cannot be reflected in the figures.

The spatial–temporal distribution and 2D Fourier transform of the air gap magnetic field in the rotor motion coordinate system are shown in Figs. 14 and 15. Since the relative magnetic permeability of the slotting effect is a function of time in rotor motion coordinate system, it can be seen from the spatial–temporal distribution that the slotting positions at different times are inconsistent, which is different from stator static coordinate system. From the results of 2D Fourier transform, it can be verified that the components of the magnetic field in rotor motion coordinate system are mainly $(0, np \pm \eta Q_s)$, $(\eta Q_s f_r, np \pm \eta Q_s)$ and so on, which are different from the components in the stationary coordinate system of the stator.

4 Experimental testing and verification

4.1 Direct measurement

The authors developed direct measurement equipment for air gap magnetic fields of rotating motors. The equipment can measure 3D spatial distribution of air gap magnetic fields on the order of 10^{-1} mm, as shown in Fig. 16. It is divided into four parts. The first part is a test platform that provides support for other parts and has a horizontal level function. The second part is a rotary table, including a base and a chuck for supporting the rotating electric machine, with positioning and high-precision rotation angle

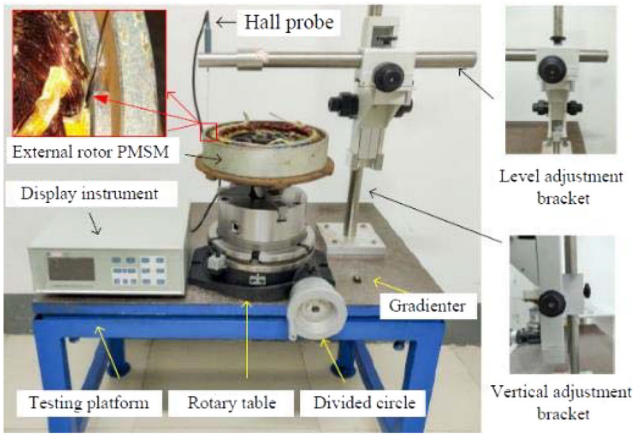

Fig. 16 *Direct measurement equipment for air gap magnetic fields*

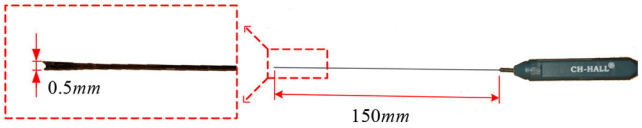

Fig. 17 *Size of hall probe*

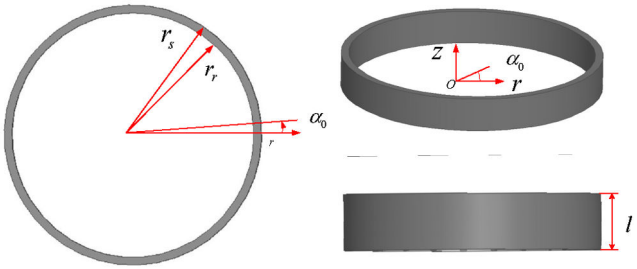

Fig. 18 *Measuring point layout*

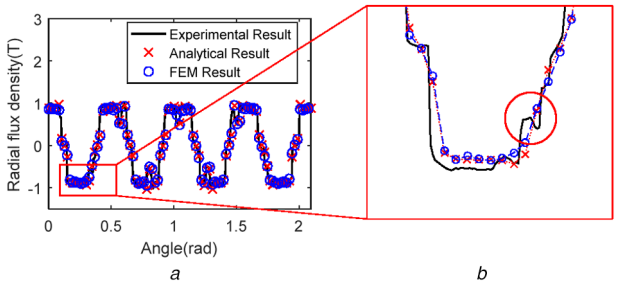

Fig. 19 *Spatial distribution of radial air gap magnetic field*
(a) Overall, ***(b)*** Local

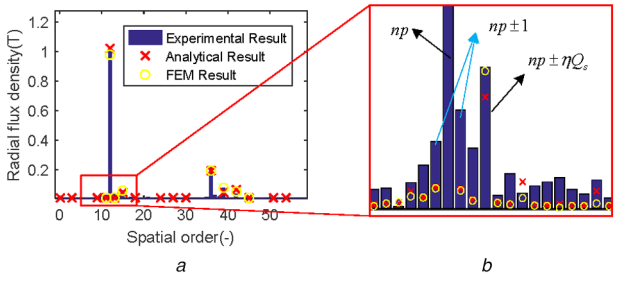

Fig. 20 *Order distribution of radial air gap magnetic field*
(a) Overall, ***(b)*** Local

adjustment. The third part is a Tesla meter, including main unit and Hall probe, used to measure the radial and tangential air gap magnetic field of the rotating machine. The fourth part is a probe holder with high precision horizontal and vertical adjustment function, for holding the Tesla meter of Hall probe.

The length, width and thickness of the hall probe are 150, 0.5 and 0.35 mm. It can be used in −196–200°C temperature range and can be extended into the air gap of the order of 10^{-1}mm for magnetic field measurement (Fig. 17).

The rotary table can realise the angle control of the order of 10^{-2} degrees, which can precisely control the rotation angle of the motor. The sensor's moving bracket enables distance control of the order of 10^{-3} mm, which precisely controls the depth of the sensor into the air gap of the motor. The combination of the two part can accurately position the sensor in the circumferential and axial directions of the air gap, which can ensure the measurement accuracy and reduce the cost.

The Hall element on the sensor is directional and can measure the radial and tangential air gap magnetic fields by rotating the probe handle to change the angular state of the Hall probe into the air gap.

Taking the geometric centre of the lower end surface of the motor stator as the coordinate origin O, the radial, circumferential angle and axial direction of the air gap ring are the r-axis, θ and z direction, respectively, the 3D cylindrical coordinate system $O-r\theta z$ is established, as shown in Fig. 18. It is known that the pole pairs number is p, the axial length is l, and the absolute value of the difference between the stator radius r_s and the rotor radius r_r is the annular columnar air gap length $g = |r_s - r_r|$. The cylindrical air gap of the motor to be tested is divided into N parts in the circumferential range of each pair of poles, and is divided into Z segments in the axial range (the larger the N and Z, the higher the precision). The segmentation point is the test case point. The adjacent operating point points are spaced apart $\alpha_0 = (360°)/2pN$ in the circumferential direction and the length $Z_0 = l/Z$ in the axial direction.

The spatial distribution results of radial air gap magnetic field can be obtained by the analytical model, finite element method (FEM) and DMT, shown as in Figs. 19 and 20. The root mean square error (RMSE) is used as the error evaluation standard. The RMSE of the analytical results and the FE results are 0.21 and 0.19, respectively. It can obviously be concluded that they agree well with the DMT results on the whole, but there are some differences at some local positions. By analysing the partial view of Fig. 19, it can be found that the DMT results can reflect the details of the magnetic field variation in some local area where the magnetic permeability changes sharply, such as the cogging tip. Meanwhile the analytical result and FEM result are smoother in the same area.

By analysing the partial view of Fig. 20, the spatial order components $np\pm1$ can clearly be observed in the DMT result, but they donot obviously appear in the analytical result and the FEM result unfortunately. It can be speculated that the tested motor may have an eccentricity fault [23, 24]. However, it cannot be distinguished whether such eccentricity is a static eccentricity with uniform axial distribution or a tilt eccentricity with uneven axial distribution. Identification of the two eccentric types will further be discussed in Section 5. From the above, there are two main reasons for this kind of difference between the calculation results and the DMT result:

(i) Both analytical and FE calculations use a series of assumptions, and have their own limitations. For example, the analytical analysis is difficult to accurately consider the non-linearity of intimate materials and the FE accuracy is limited by the meshing quality and quantity.

(ii) During the in-wheel motor production, manufacturing and assembly process, unpredictable failures might occur. Additionally, some faults may appear because of complex installation conditions and stress environment of the in-wheel motors. However, because these kinds of failures and faults are not diagnosed, they are ignored during the modelling and calculating process. For example, in this study, the eccentric fault of the tested motor might have an eccentricity fault according to the spatial order components $np\pm1$ of the air gap magnetic field in the DMT result.

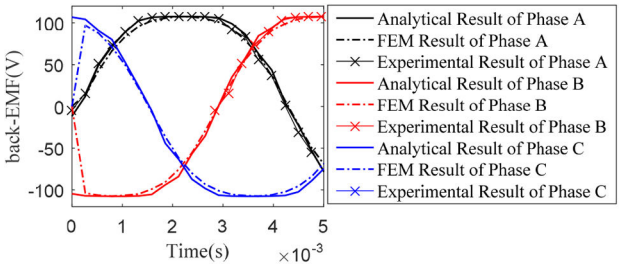

Fig. 21 *Experimental verification of no-load back EMF*

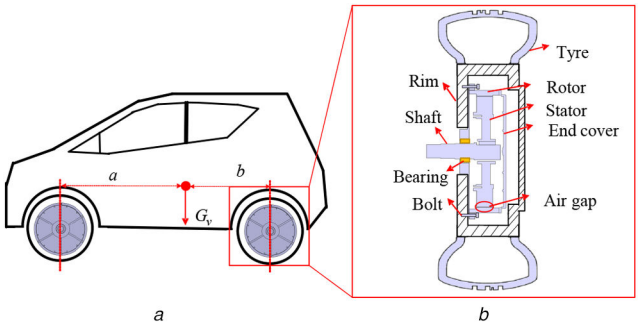

Fig. 22 *Installation location and structure of motor*
(a) Vehicle, ***(b)*** In-wheel motor

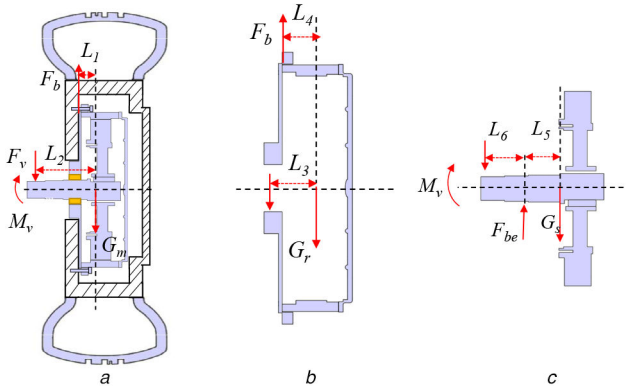

Fig. 23 *Force analyses*
(a) Motor, ***(b)*** Rotor assembly, ***(c)*** Stator assembly

4.2 Indirect measurement

The no-load back EMF measurement is simple and the method is mature. It can generally be used to detect the accuracy of the air gap magnetic field analytical calculation and FE calculation. Based on the analysis of the no-load air gap magnetic field in Section 2, the Faraday's law can be used to calculate the no-load back EMF [24]. In this study, the analytical calculation results and the FE calculation results are verified by the three-phase line back EMF measured by experimental test, as shown in Fig. 21. It can be seen that the three have a high degree of coincidence, so the accuracy of the no-load air gap magnetic field calculation can be verified.

5 Mechanical and magnetic challenges of in-wheel motors

5.1 Formation of tilt eccentricity

Although the electric vehicle driven by the in-wheel motor has the advantages of high transmission efficiency and fast control response, its unsprung mass and the dynamic load of tyres increase. As a result, its ride comfort and handling stability may deteriorate. Because the in-wheel motor rigidly connects to the wheel hub and directly bears severe body load and road excitation, it might deform in the axial direction [24]. Consequently, the air gap of the in-wheel motor might further become uneven in circumferential and axial directions and its air gap magnetic field distortion occurs seriously. In this study, only static deformation of the in-wheel motor is considered according to the static eccentricity fault detection of the air gap magnetic field in Section 4.1.

Table 5 Structural parameters of vehicle and motor

Items	Symbol	Values/unit
vehicle mass	M_v	1343/kg
stator assembly mass	S_m	9.19/kg
rotor assembly mass	R_m	8.78/kg
distance between centre of vehicle mass and front axle	A	1.158/m
distance between centre of vehicle mass and rear axle	B	1.147/m
distance between centre of motor and bolts	L_1	38.3/mm
distance between centre of motor and frame	L_2	97.3/mm
distance between centre of rotor assembly mass and bearing	L_3	37.56/mm
distance between centre of rotor assembly mass and bolts	L_4	29.55/mm
distance between centre of stator assembly mass and bearing	L_5	47.82/mm
distance between frame and bearing	L_6	55/mm

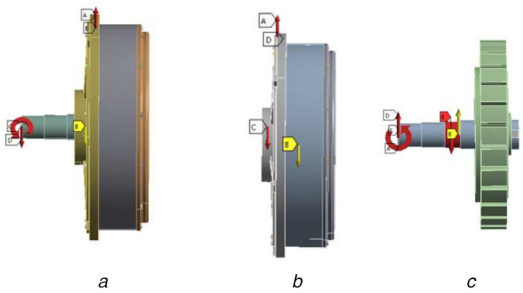

Fig. 24 *Static analyses*
(a) Motor, ***(b)*** Rotor assembly, ***(c)*** Stator assembly

An electric vehicle driven by four in-wheel motors is shown in Fig. 22. Each motor directly connects to a wheel hub and is supported by a single-sided bearing.

The force analyses of the in-wheel motor, the stator assembly and the rotor assembly are shown in Fig. 23. The force balance expressions are given as (6)–(11).

$$F_{\mathrm{b}} = G_{\mathrm{m}} + F_{\mathrm{v}} \tag{6}$$

$$F_{\mathrm{b}}L_1 + M_{\mathrm{v}} = F_{\mathrm{v}}L_2 \tag{7}$$

$$F_{\mathrm{b}} = G_{\mathrm{r}} + F_{\mathrm{be}} \tag{8}$$

$$F_{\mathrm{b}}L_4 = F_{\mathrm{be}}L_3 \tag{9}$$

$$F_{\mathrm{be}} = G_{\mathrm{s}} + F_{\mathrm{v}} \tag{10}$$

$$G_{\mathrm{s}}L_5 + M_{\mathrm{v}} = F_{\mathrm{v}}L_6 \tag{11}$$

where F_{b}, F_{v}, F_{be}, M_{v} are bolt force, frame force, bearing force and frame moment, respectively. G_{m}, G_{r}, G_{s} are gravities of the motor, the rotor assembly and the stator assembly, respectively.

The structural parameters of the vehicle and the motor are shown in Table 5. The magnitude of each force can be calculated by substituting the parameters into (6)–(11).

Loads and constraints are set in ANSYS, as shown in Fig. 24, and the static deformation of the motor is calculated. The static deformation results of the motor are shown in Fig. 25*a*. In this case, the static force transmitted from the frame to the shaft end is 3360 N. When considering the mass of passengers, the total mass increased by about 300 kg, and the shaft end is subjected to 4118 N. In this case, the static deformation results of motor are shown in Fig. 25*b*.

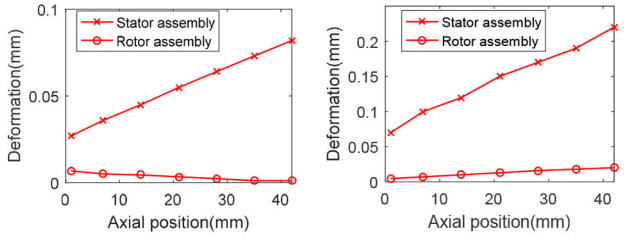

Fig. 25 *Deformation of stator/rotor assembly in the axial direction*
(a) No-load mass, ***(b)*** Full load mass

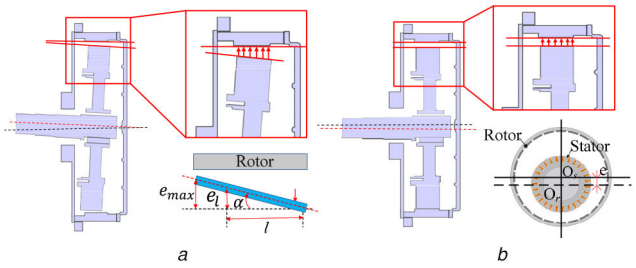

Fig. 26 *Eccentric fault diagram*
(a) Tilt eccentricity, ***(b)*** Static eccentricity

As can be seen from Fig. 25*a*, when the vehicle is under no load mass, the stator/rotor assembly will deform in the axial direction. Among them, the stator assembly mainly deforms, its maximum deformation is 0.082 mm, and its corresponding static eccentricity ratio is 10.25%, which is still within the acceptable range. When the vehicle is under full load mass, the eccentricity ratio of the maximum deformation deformation is 27.5%, and the in-wheel motor has a significant axial tilt eccentricity. Therefore, the tilt eccentricity problem caused by the mechanical challenge of in-wheel motors cannot be ignored.

5.2 Analytical model of tilt eccentricity

For the tilt eccentricity of the in-wheel motor, the air gap unevenly distributes both in the circumferential direction and the axial direction, and the degree of eccentricity at each axial position is different. In the cross section of each axial position, the tilt eccentricity can be considered as a kind of the static eccentricity with different eccentric degree, shown in Fig. 26*a*.

The eccentricity ratio $\varepsilon(l)$ at each axial position is defined

$$\varepsilon(l) = \frac{e_l}{\delta} = \frac{e_{\max} l}{\delta L \cos\alpha} \tag{12}$$

where e_l and $e_{\max}$ are the eccentric distances at an axial position l and the maximum eccentricity axial position, respectively. δ is the equivalent air gap length, L is the axial length of the motor and α is the tilt eccentricity angle.

Based on permeability correction coefficient of static eccentricity [23, 24] and the change of the eccentricity of the motor in axial direction, the analytical expression of the permeability correction coefficient of the tilt eccentricity can be derived as follows:

$$\varepsilon(l,\theta) = \frac{1}{1-\varepsilon(l)\cos\theta} = \sum_{v=0}^{\infty} \varepsilon_v \cos(v\theta) \tag{13}$$

Taking the first two orders of the Fourier series, the expression is as follows:

$$\begin{aligned}\varepsilon(l,\theta) &= \varepsilon_0 + \varepsilon_1\cos\theta \\ &= \frac{1}{\sqrt{1-\varepsilon^2(l)}} + \frac{2}{\sqrt{1-\varepsilon^2(l)}}\left(\frac{1-\sqrt{1-\varepsilon^2(l)}}{\varepsilon(l)}\right)\cos\theta\end{aligned} \tag{14}$$

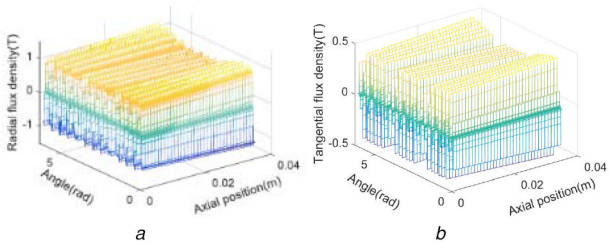

Fig. 27 *Magnetic flux density circumferential and axial distribution*
(a) Radial, ***(b)*** Tangential

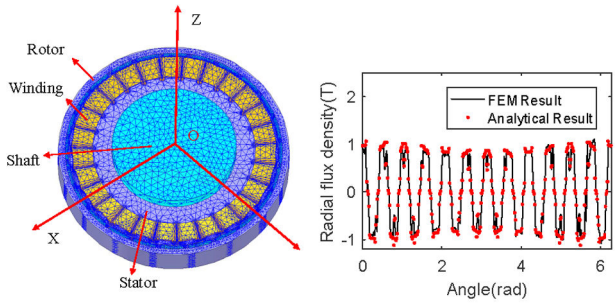

Fig. 28 *3D-FE model and results*
(a) Model, ***(b)*** Result

In the same way, the permeability correction coefficient of tilt eccentricity in rotor coordinate system can be obtained as

$$\begin{aligned}\varepsilon(l,\theta) = \varepsilon_0 + \varepsilon_1\cos(\omega t+\varphi+\theta) &= \frac{1}{\sqrt{1-\varepsilon^2(l)}} \\ &+ \frac{2}{\sqrt{1-\varepsilon^2(l)}} \times \left(\frac{1-\sqrt{1-\varepsilon^2(l)}}{\varepsilon(l)}\right)\cos(\omega t+\varphi+\theta)\end{aligned} \tag{15}$$

By multiplying the analytical expressions (1)–(4) of the magnetic flux density in stator and rotor coordinate systems with (14) and (15), respectively, the distribution of air gap flux density along the circumference and axial direction can be obtained under tilt eccentricity.

It can be seen from (14) that in stator coordinate system, the tilt eccentricity does not affect the frequency characteristics of the air gap magnetic density, but it leads to $a\pm1$ spatial order characteristic. While in the rotor coordinate system in (15), the tilt eccentricity affects both the frequency characteristics ($\pm f_r$) and the spatial order (±1) of the air gap magnetic density.

The circumferential and axial distributions of the no-load air-gap magnetic density are calculated analytically, as shown in Fig. 27. A 3D electromagnetic FE model of the motor is proposed as well in Fig. 28*a*. The analytical result and the FEM result of the spatial distribution magnetic density at the axial position $l = 33$ mm are compared in Fig. 28*b*. They agree well with each other.

It is worth noting that when analysing the axially non-uniform air-gap magnetic field, the 3D model established by general electromagnetic FE tools is often very time-consuming. The no-load FE static magnetic field simulation used in this study takes 90 min, and the analytical model only takes 20 s, under the same hardware environment. Therefore, the calculation speed advantage of the analytical model in 3D analysis is more obvious.

5.3 Fault detection of tilt eccentricity based on DMT

During the in-wheel motor production, manufacturing and assembly process, unpredictable failures might occur. Additionally, some faults may appear because of complex installation conditions and stress environment of the in-wheel motors. However, because these kinds of failures and faults are not diagnosed, they are ignored during the modelling and calculating process. No matter it is the FEM or the analytical method, it can only simulate the motors with known specific faults, but it cannot detect a motor with an unknown fault.

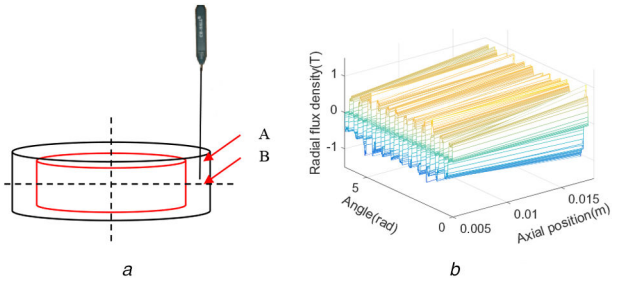

Fig. 29 *Measuring points and results of axial distribution of magnetic field*
(a) Measure point, ***(b)*** Results

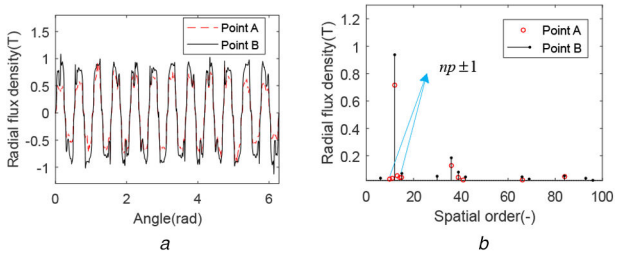

Fig. 30 *Comparison of the flux density at two axial locations*
(a) Amplitude, ***(b)*** Frequency spectrum

The tilt eccentricity is a typical fault for an in-wheel motor. However, it is still difficult to distinguish whether such eccentricity is a static eccentricity with uniform axial distribution or a tilt eccentricity with uneven axial distribution according to the spatial order components $np\pm1$ of the air gap field. In order to effectively distinguish the two types of eccentric faults, the fault detection of tilt eccentricity based on DMT is proposed as follows.

On one hand, if an in-wheel motor has a static eccentricity with uniform axial distribution, the magnetic field amplitude and eccentricity ratio in the cross section of each different axial position are the same. On the other hand, if the in-wheel motor has tilt eccentric fault, its air gap length changes along the axial direction, and further the magnetic field amplitudes and eccentricity ratios at different axial positions are different. Therefore, DMT can be used to measure the air gap magnetic field distribution in the cross sections of different axial positions, shown in Fig. 29*a*. Then, the amplitudes of magnetic field and eccentricity ratios at different axial positions can be obtained and compared, shown in Fig. 29*b*. If they are not the same, the fault is judged as the tilt eccentric fault.

Comparing the air gap magnetic circumferential distribution waveforms and order characteristics at two axial locations, as shown in Figs. 30*a* and *b*, the following characteristics are obtained:

(i) The amplitudes of magnetic field at two axial positions of the in-wheel motor are greatly different.
(ii) The eccentric characteristic component $np\pm1$ of the air gap magnetic field at both of the axial positions appear, but their characteristic amplitudes are different and their degree of eccentricities are different.

Based on the above characteristics, it can be determined that the tested motor has a tilt eccentricity fault.

6 Conclusion

The main conclusions are as follows:

(i) In stator static coordinate system, the spatial order of air gap magnetic density of external rotor PMSMs with PWM technique is np, $np\pm\eta Q_s$, vm and $vm\pm\eta Q_s$, the frequency characteristics are nf_c, $(3h\pm1)f_c$ and $k_1f_s\pm k_2f_c$. New spatial orders are introduced by the stator slotting effect.

(ii) In rotor motion coordinate system, the spatial order of the air gap magnetic density of external rotor PMSMs with PWM technique is the same as that in stator static coordinate system, and the frequency characteristics change to 0, $\eta Q_s f_r$, $(3h\pm1)f_c\pm vf_r$ and $(3h\pm1)f_c\pm(v\pm\eta Q_s f_r)$ due to the influence of the stator slotting.
(iii) The application scenarios of in-wheel motors may cause a serious axial tilt eccentricity fault, which distorts the air gap magnetic field and affects the electromagnetic performance of the motors.
(iv) The DMT proposed in this study can detect the precise distribution and can also be used for the tilt eccentric fault diagnosis.

7 References

[1] Zhu, Z.Q., Xia, Z., Wu, L., *et al.*: 'Analytical modeling and finite-element computation of radial vibration force in fractional-slot permanent-magnet brushless machines', *IEEE Trans. Ind. Appl.*, 2010, **46**, (5), pp. 1908–1918

[2] Rahideh, A., Korakianitis, T.: 'Analytical calculation of open-circuit magnetic field distribution of slotless brushless PM machines', *Int. J. Electr. Power Energy Syst.*, 2013, **44**, (1), pp. 99–114

[3] Rahideh, A., Korakianitis, T.: 'Analytical magnetic field distribution of slotless brushless PM motors. Part 2: open-circuit field and torque calculations', *IET Electr. Power Appl.*, 2012, **6**, (9), pp. 639–651

[4] Liang, P., Chai, F., Li, Y., *et al.*: 'Analytical prediction of magnetic field distribution in spoke-type permanent-magnet synchronous machines accounting for bridge saturation and magnet shape', *IEEE Trans. Ind. Electron.*, 2017, **64**, (5), pp. 3479–3488

[5] Pourahmadi-Nakhli, M., Rahideh, A., Mardaneh, M.: 'Analytical 2-D model of slotted brushless machines with cubic spoke-type permanent magnets', *IEEE Trans. Energy Convers.*, 2018, **33**, (1), pp. 373–382

[6] Zhu, Z.Q., Howe, D.: 'Instantaneous magnetic field distribution in permanent magnet brushless dc motors, part IV: magnetic field on load', *IEEE Trans. Magn.*, 1993, **29**, (1), pp. 152–158

[7] Zhu, Z.Q., Howe, D.: 'Instantaneous magnetic field distribution in permanent magnet brushless dc motors, part I: open-circuit field', *IEEE Trans. Magn.*, 1993, **29**, (1), pp. 124–135

[8] Ma, C.G., Chen, C.Y., Li, Q., *et al.*: 'Analytical calculation of No-load magnetic field of external rotor permanent magnet brushless direct current motor used as In-wheel motor of electric vehicle', *IEEE Trans. Magn.*, 2018, **54**, (4), pp. 1–6

[9] Zarko, D., Ban, D., Lipo, T. A.: 'Analytical calculation of magnetic field distribution in the slotted air gap of a surface permanent-magnet motor using complex relative air-gap permeance', *IEEE Trans. Magn.*, 2006, **42**, (7), pp. 1828–1837

[10] Zhu, Z.Q., Howe, D.: 'Instantaneous magnetic field distribution in permanent magnet brushless dc motors, part II: armature-reaction field', *IEEE Trans. Magn.*, 1993, **29**, (1), pp. 136–142

[11] Zhu, Z.Q., Howe, D.: 'Instantaneous magnetic field distribution in permanent magnet brushless dc motors, part III: effect of stator slotting', *IEEE Trans. Magn.*, 1993, **29**, (1), pp. 143–151

[12] Ma, C.G., Li, Q., Lu, H.F., *et al.*: 'Analytical model for armature reaction of outer rotor brushless permanent magnet DC motor', *IET Electr. Power Appl.*, 2018, **12**, (5), pp. 651–657

[13] Lin, F., Zuo, S.G., Wu, X.D.: 'Electromagnetic vibration and noise analysis of permanent magnet synchronous motor with different slot-pole combinations', *IET Electr. Power Appl.*, 2016, **10**, (9), pp. 900–908

[14] Zuo, S.G., Lin, F., Wu, X.D.: 'Noise analysis, calculation, and reduction of external rotor permanent-magnet synchronous motor', *IEEE Trans. Ind. Electron.*, 2015, **62**, (10), pp. 6204–6212

[15] Krotsch, J., Piepenbreier, B.: 'Radial forces in external rotor permanent magnet synchronous motors with non-overlapping windings', *IEEE Trans. Ind. Electron.*, 2012, **59**, (5), pp. 2267–2276

[16] Ajily, E., Ardebili, M., Abbaszadeh, K.: 'Magnet defect and rotor eccentricity modeling in axial-flux permanent-magnet machines via 3-D field reconstruction method', *IEEE Trans. Energy Convers.*, 2016, **31**, (2), pp. 486–495

[17] Zhu, Z.Q., Wu, L., Mohd Jamil, M.L.: 'Distortion of back-EMF and torque of PM brushless machines due to eccentricity', *IEEE Trans. Magn.*, 2013, **49**, (8), pp. 4927–4936

[18] Mystkowski, A., Kierdelewicz, A., Jastrzebski, R.P., *et al.*: 'Flux measurement and conditioning system for heteropolar active magnetic bearing using kapton-foil hall sensors', *Mech. Syst. Signal Process.*, 2019, **115**, (1), pp. 394–404

[19] Mirzaeva, G., Saad, K.I.: 'Advanced diagnosis of rotor faults and eccentricity in induction motors based on internal flux measurement', *IEEE Trans. Ind. Appl.*, 2018, **54**, (3), pp. 2981–2991

[20] Haller, S., Cheng, P., Oelmann, B.: 'Air-gap flux density measurement system for verification of permanent magnet motor FEM model'. IECON 2015-41st Annual Conf. of the IEEE Industrial Electronics Society IEEE, Yokohama, Japan, 2015, pp. 000445–000450

[21] Saadoun, A., Amirat, Y.: 'Magnetic flux density measurement in permanent magnet synchronous machines'. Int. Conf. on Sciences & Techniques of Automatic Control & Computer Engineering IEEE, Monastir, Tunisia, 2015, pp. 355–359

[22] Deng, W.Z., Zuo, S.G.: 'Comparative study of sideband electromagnetic force in internal and external rotor PMSMs with SVPWM technique', *IEEE Trans. Ind. Electron.*, 2019, **66**, (2), pp. 956–966
[23] Ma, C.G., Cui, H.W., Zheng, P.*, et al.*: 'Infuence of static eccentricity on unbalanced magnetic force of external rotor permanent magnet brushless direct current motor used as in-wheel motor', *IET Electr. Power Appl.*, 2019, **13**, (4), pp. 538–550
[24] Zuo, S.G., Zhang, G.H., Wu, X.D.*, et al.*: 'Analysis of electromagnetic force in wheel-drive PMSM with stator incline eccentricity', *J. Zhejiang Univ. (Eng. Sci.)*, 2015, **49**, (5), pp. 901–907